Al0.2Ga0.8As 2 × 2 square pixel X-ray photodiode array

Article (Published Version)

Nuclear Inst. and Methods in Physics Research, A 899 (2018) 106–114

Contents lists available at ScienceDirect

Nuclear Inst. and Methods in Physics Research, A

journal homepage: www.elsevier.com/locate/nima

$Al_{0.2}Ga_{0.8}As$ 2 × 2 square pixel X-ray photodiode array

M.D.C. Whitaker *, G. Lioliou, A.M. Barnett

Space Research Group, Sch. of Engineering and Informatics, University of Sussex, Falmer, Brighton, BN1 9QT, UK

ARTICLE INFO

Keywords:
AlGaAs
X-ray detector
Spectroscopy
Photodiode
Array
Semiconductor

ABSTRACT

A monolithic 2 × 2 square pixel $Al_{0.2}Ga_{0.8}As$ p^+–i–n^+ mesa X-ray photodiode array (each photodiode area 200 μm by 200 μm, 3 μm i layer) has been fabricated from material grown by MOVPE. The array was electrically characterised across the temperature range 100 °C to -20 °C. Each pixel's response to illumination with soft X-rays from an ^{55}Fe radioisotope X-ray source (Mn Kα = 5.9 keV; Mn Kβ = 6.49 keV) was investigated across the temperature range 30 °C to -20 °C. The best energy resolution (FWHM at 5.9 keV) achieved at 20 °C was 0.76 keV ± 0.06 keV (with 30 V reverse bias applied to the detector). The measured energy resolution is the best so far reported for AlGaAs X-ray photodiodes at 20 °C. It is also the first time a small AlGaAs X-ray photodiode array has been demonstrated. Due to the temperature tolerance and the radiation hardness of AlGaAs, such detectors are expected to find utility in future space science missions exposed to intense radiation environments, for example missions to study the Jovian or Saturnian aurorae and high temperature planetary surfaces.

1. Introduction

Conventional Si and Ge X-ray spectrometers often require significant shielding and cooling mechanisms in order to function in extreme environments (e.g. temperatures ≫ 20 °C). For space science instrumentation and certain terrestrial applications, mass, volume, and power consumption are of critical importance. As such, technologies which enable the reduction of the requirements for these aspects are potentially very attractive. $Al_xGa_{1-x}As$ has received particular attention as a promising material for X-ray [1–4] and beta particle [5,6] detection, with uncooled operation at room temperature, and above, having been successfully demonstrated. The relatively wide bandgap of $Al_xGa_{1-x}As$ (e.g. 1.67 eV for $x = 0.2$) [7] enables superior energy resolutions at high temperature as a result of lower thermally induced leakage currents compared with narrower bandgap devices [8]. In addition, the larger X-ray linear attenuation coefficient of $Al_xGa_{1-x}As$ (e.g. 787.8 cm^{-1} for $Al_{0.2}Ga_{0.8}As$ cf. 346.4 cm^{-1} for Si, at 5.9 keV) [9] allows for use of thinner detectors. The expected better radiation hardness of $Al_xGa_{1-x}As$ [10–12] is also anticipated to be useful in intense radiation environments such as those encountered in missions to study the Jovian [13,14] or Saturnian [15] aurorae, or to study X-ray emissions from Jupiter's Galilean moons [16]; where improved detector durability could increase mission lifetime in addition to reducing mission costs. To date, progress in AlGaAs detectors has been impeded due to poor device yields. However, here, for the first time, it is demonstrated that yields are now sufficient that small (2 × 2) mesa pixel arrays can be produced with good enough quality that they are suitable for photon counting X-ray spectroscopy.

Previously, prototype single pixel $Al_xGa_{1-x}As$ photodiodes of varying Al concentration have been characterised and reported. $Al_{0.2}Ga_{0.8}As$ circular mesa p^+–i–n^+ photodiodes (200 μm diameter, 3 μm i layer) have been subject to study across the temperature range 60 °C to −20 °C [4] and characterised as soft X-ray photon counting detectors, with an energy resolution (Full Width at Half Maximum, FWHM) of 1.06 keV at 5.9 keV at room temperature for the best performing diode [4]. Similarly, single pixel $Al_{0.8}Ga_{0.2}As$ circular mesa p^+–i–n^+ photodiodes (200 μm diameter, 1 μm i layer) have been characterised as soft X-ray photon counting detectors, with an energy resolution (FWHM) of 1.07 keV at 5.9 keV reported at room temperature for the best performing diode [17]. Larger area devices (400 μm diameter) with thicker epilayers (1.7 μm) have also been reported with a mean leakage current density of 4.72 nA cm^{-2} ± 1.67 nA cm^{-2} at an average electric field strength of 29.4 kV/cm (5 V operating reverse bias), and a mean energy resolution (FWHM) of 1.27 keV at 5.9 keV at room temperature [2]. Although single pixel detectors are useful for many applications, for other applications, pixel arrays are more desirable. In this article, the electrical characterisation of a 2 × 2 square pixel $Al_{0.2}Ga_{0.8}As$ array is reported over a temperature range of 100 °C to −20 °C, and their performance as spectroscopic photon counting X-ray detectors was characterised over the temperature range 30 °C to −20 °C.

* Corresponding author.
E-mail address: M.Whitaker@sussex.ac.uk (M.D.C. Whitaker).

https://doi.org/10.1016/j.nima.2018.05.032
Received 8 February 2018; Received in revised form 14 May 2018; Accepted 14 May 2018
Available online 17 May 2018

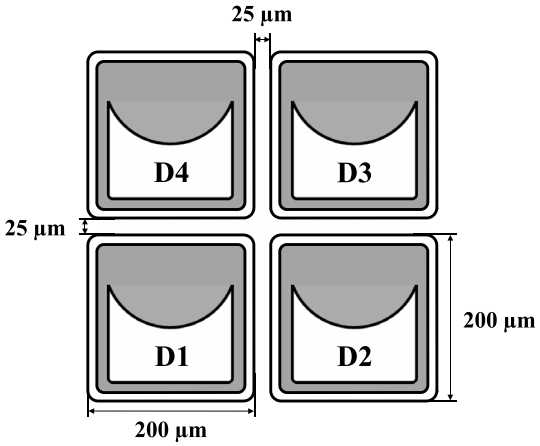

Fig. 1. Layout of the $Al_{0.2}Ga_{0.8}As$ p^+–i–n^+ mesa X-ray photodiode 2 × 2 array, where the shaded area is the top contact/bondpad.

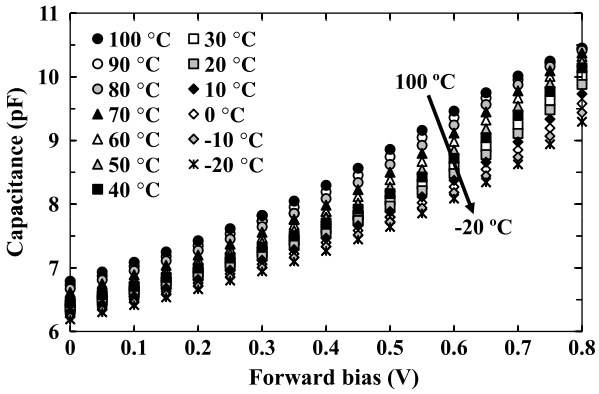

Fig. 2. Capacitance as a function of applied forward bias for pixel D1 in the temperature range 100 °C to −20 °C. Comparable results were obtained for pixels D2, D3, and D4.

Table 1
Layer details of the $Al_{0.2}Ga_{0.8}As$ p^+–i–n^+ structure from which the devices were fabricated.

Material	Dopant	Dopant type	Thickness (nm)	Doping density (cm^{-3})
GaAs	Be	p	10	1×10^{19}
$Al_{0.2}Ga_{0.8}As$	Be	p	500	2×10^{18}
$Al_{0.2}Ga_{0.8}As$			3000	Undoped
$Al_{0.2}Ga_{0.8}As$	Si	n	1000	2×10^{18}
GaAs n^+ substrate				

2. Diode design

An $Al_{0.2}Ga_{0.8}As$ p^+–i–n^+ structure was grown by metalorganic vapour phase epitaxy (MOVPE) on a commercial 2 inch GaAs n^+ substrate. The layer details are summarised in Table 1. Square, 200 µm× 200 µm, mesa structures were formed using 1:1:1 H_3PO_4:H_2O_2:H_2O solution followed by 10 s in 1:8:80 H_2SO_4:H_2O_2:H_2O solution. An Ohmic contact consisting of 20 nm InGe and 200 nm Au was evaporated onto the rear of the substrate, and an Ohmic top contact of 20 nm Ti and 200 nm Au was evaporated onto the p^+ side of the mesa devices; the devices were unpassivated. Fig. 1 illustrates the geometry of the pixels. The p^+ metal contact is represented by the shaded area, it covers 50% of each pixel's surface. The devices were packaged in a TO-5 can.

3. Experimental results

3.1. Capacitance as a function of applied bias

Capacitance as a function of applied forward and reverse bias was measured for each $Al_{0.2}Ga_{0.8}As$ p^+–i–n^+ pixel (D1, D2, D3, and D4) across the temperature range 100 °C to −20 °C, using an HP 4275A LCR Meter (signal magnitude 50 mV rms; frequency 1 MHz) and a Keithley 6487 picoammeter/voltage source to bias the detectors. The light-tight dark electromagnetically screened test harness, in which the $Al_{0.2}Ga_{0.8}As$ detectors were installed, was placed inside a TAS Micro MT climatic cabinet for temperature control and a thermocouple appropriately positioned in order to monitor the temperature and ensure that thermal equilibrium was reached and maintained between the climatic cabinet and the detectors at each temperature. The test harness was purged with dry N_2 and the climatic cabinet closed. The climatic cabinet was continually purged with dry N_2 for the duration of the measurement in order to eliminate any humidity related effects [18]. National Instruments LabVIEW software was used to automate the characterisation routine. The temperature was initially set to 100 °C, and then decreased in 10 °C steps to −20 °C, with measurements made at each step. The diodes were left for 30 min after reaching each temperature before measuring in order to ensure thermal equilibrium and stabilisation. Since the devices were measured after packaging, the capacitance of the package was estimated and removed by measuring the capacitance of an empty connection from an identical package across the same applied bias range and at each temperature. The packaging capacitance values were then deducted from the respective packaged device capacitances obtained for the detectors. Temperatures greater than 100 °C were not measured due to the high leakage currents (>1 nA at 15 V at 120 °C) observed at such temperatures. Fig. 2 presents the capacitance of photodiode, D1, with the packaging capacitance subtracted, as a function of applied forward bias; comparable results were found for D2, D3, and D4.

As the temperature was decreased from 100 °C to −20 °C, the forward capacitance decreased at each applied forward bias. At 100 °C and at an applied forward bias of 0.8 V, capacitances of 10.45 pF, 10.60 pF, 10.62 pF, 10.41 pF (each ± 0.05 pF) were measured for D1, D2, D3, and D4 respectively. At −20 °C and at the same applied forward bias, capacitances of 9.29 pF, 9.40 pF, 9.43 pF, 9.26 pF (each ± 0.05 pF) were measured. The diffusion capacitance, a consequence of the change in minority carrier density, significantly contributed to the diode forward capacitance. Since the diffusion capacitance is directly proportional to the forward current [19], the observed dependency of the forward capacitance with temperature (Fig. 2) was attributed to the same temperature dependence of the forward current (see Section 3.2).

The capacitance for D1 as a function of applied reverse bias in the temperature range 100 °C to −20 °C can be seen in Fig. 3. Comparable results were found for D2, D3, and D4. At low applied reverse biases, the measured capacitances decreased as the temperature decreased: without application of reverse bias (i.e. at 0 V applied bias) and at 100 °C, capacitances of 6.77 pF, 6.85 pF, 6.88 pF, and 6.73 pF (each ± 0.04 pF) were measured for D1, D2, D3, and D4, respectively; at −20 °C, capacitances of 6.19 pF, 6.26 pF , 6.29 pF, and 6.14 pF (each ± 0.04 pF) were measured. As the applied reverse bias was increased in magnitude, the temperature dependence of the capacitance reduced at that applied reverse bias; at applied reverse biases ≥ 7 V, any variation in capacitance as a function of temperature became indiscernible i.e. the change in capacitance remained within the uncertainty of the measurement, as shown by Fig. 3.

When reverse biased, the junction capacitance was predominantly defined by the depletion layer capacitance, $C_{DL}(V_R)$ [19]. Thus, from the measured depletion layer capacitance $C_{DL}(V_R)$, the depletion width as a function of applied reverse bias $W(V_R)$ was calculated using,

$$C_{DL}\left(V_R\right) = \frac{\varepsilon_0 \varepsilon A}{W\left(V_R\right)}, \tag{1}$$

where ε_0 was the permittivity of free space, ε was the relative permittivity of the material (12.332 for $Al_{0.2}Ga_{0.8}As$ [20]), and A was the

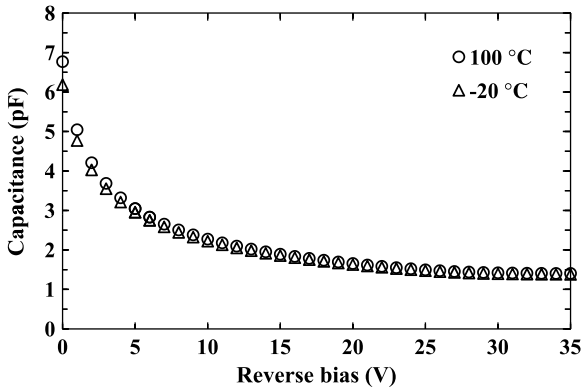

Fig. 3. Capacitance as a function of reverse bias for pixel D1, at 100 °C (circles) and −20 °C (triangles). Comparable results were obtained for pixels D2, D3, and D4.

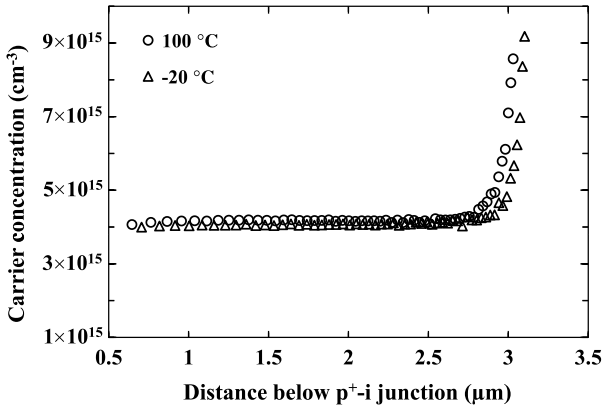

Fig. 5. Doping profile for D1, at 100 °C (circles) and −20 °C (triangles). Comparable results were obtained for D2, D3, and D4. The variation of the carrier concentration between 100 °C and −20 °C fell within the calculated uncertainty of the measurements.

area of the device [19]. The Debye length of $Al_{0.2}Ga_{0.8}As$ (0.07 μm) was calculated as per Ref. [21] and was taken into account when calculating the depletion width uncertainty. The depletion width of each diode increased as a function of applied reverse bias at all temperatures, until a reverse bias of 26 V, at which the i layer of each pixel was fully depleted. At high reverse biases (≥26 V), the depletion width of each pixel was found to be temperature independent; any apparent variation in calculated depletion width as a function of temperature lay within the measurement uncertainty. For D1, at the hottest investigated temperature, 100 °C, the depletion width was 0.65 μm ± 0.07 μm at 0 V, and 3.11 μm ± 0.10 μm at 35 V. Comparable results were obtained for the other pixels. The calculated depletion width as a function of applied reverse bias at −20 °C and 100 °C for pixel D1, and the quantum detection efficiency implied by this width assuming that the active region of the photodiodes was solely confined to the depletion region, and that only the depleted part of the i layer was active, can be seen in Fig. 4. The quantum detection efficiency of the $Al_{0.2}Ga_{0.8}As$ X-ray p–i–n mesa pixels at an applied reverse bias of 30 V was 0.21 at 5.9 keV and 0.17 at 6.49 keV in areas not covered by the top contact, and 0.17 at 5.9 keV and 0.14 at 6.49 keV in areas covered by the top contact. It should be noted that this is a conservative assumption since it is likely that at least some of the charge carriers created in the non-depleted part of the i layer also contributed to the collected charge at lower reverse biases. Furthermore, previous investigations have shown that electrons from electron–hole pairs created in the p region and within 0.16 μm of the p–i interface in $Al_{0.8}Ga_{0.2}As$ X-ray photodiodes, also contribute to the detected signals [22].

The carrier concentration of the i layer, $N(W)$, was calculated using the equation for general nonuniform distributions,

$$\frac{\mathrm{d}\left(1/C_{DL}^2\right)}{\mathrm{d}V_R} = \frac{2}{\mathrm{q}\varepsilon_0\varepsilon N(W)}, \tag{2}$$

where q is the elementary charge [19]. The carrier concentration throughout the intrinsic region was calculated to be 4×10^{15} cm^{-3} for each pixel. At the i–n$^+$ interface, the carrier concentration increased to 2×10^{18} cm^{-3} for each pixel. The carrier concentration as a function of distance, W, below the p$^+$-i junction for D1 has been plotted in Fig. 5. Although there appears to be some carrier concentration variation with temperature, this was within the calculated uncertainty of the measurements.

3.2. Current as a function of applied bias

Current as a function of applied forward and reverse bias across the temperature range 100 °C to −20 °C was measured using a Keithley 6487 Picoammeter/Voltage Source. Each diode was housed

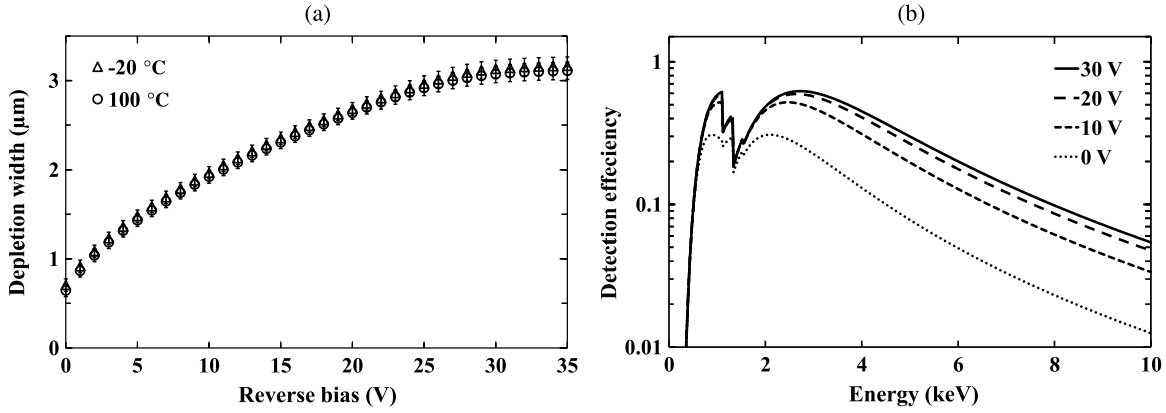

Fig. 4. (a) Calculated depletion width as a function of reverse bias for D1, at −20 °C (triangles) and 100 °C (circles). Comparable results were obtained for D2, D3, and D4. (b) Calculated detection efficiency as a function of energy for the $Al_{0.2}Ga_{0.8}As$ X-ray p–i–n mesa pixels when operated at: 30 V (solid line), 20 V (long dashed line), 10 V (short dashed line), and 0 V (dotted line) reverse bias, respectively, assuming that the active region of the photodiodes in each case was confined solely to the depletion region and that only the depleted part of the i layer was active. It should be noted that this is a conservative assumption, since it is likely that charge carriers created in the non-depleted part of the i layer also contribute to the collected charge. The p$^+$ layer was considered to be inactive and the top contact was excluded from the QE calculations. The discontinuities are the Al K, Ga L, and As L X-ray absorption edges.

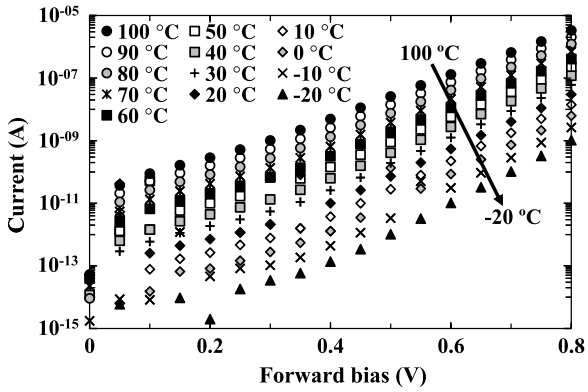

Fig. 6. Current as a function of applied forward bias in the temperature range 100 °C to −20 °C for pixel D1. Comparable results were obtained for pixels D2, D3, and D4.

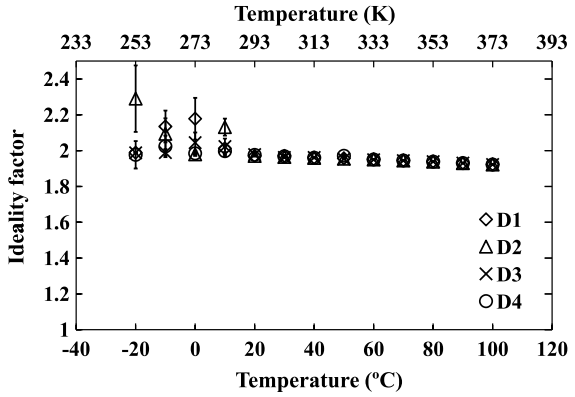

Fig. 7. Ideality factor as a function of temperature, extracted from the measured current as a function of applied forward bias ($0.5 \leq V_f \leq 0.8$) for pixels D1 (diamonds), D2 (triangles), D3 (crosses), and D4 (circles).

in a custom light-tight electromagnetically screened test harness and installed within a TAS Micro MT climatic cabinet for temperature control. As for the capacitance measurements, the test harness was initially purged with dry N_2, then the climatic cabinet was closed. The climatic cabinet was continually purged with dry N_2 for the duration of the measurements to eliminate any humidity related effects [18]. The temperature was initially set to 100 °C and decreased in 10 °C increments to −20 °C. The diodes were left to stabilise for 30 min at each temperature before measuring to ensure thermal equilibrium. Fig. 6 presents the dark current, I_F, as a function of applied forward bias for diode, D1. At each bias, the dark current decreased as the temperature was decreased. Comparable results were obtained for D2, D3, and D4.

The saturation current, I_0, and ideality factor, n, were calculated at each temperature, based on the linear region of the semi-logarithm I–V characteristics as described in Refs. [18] and [23] and the equation

$$I_F = I_0 exp\left(\frac{qV_F}{nkT}\right), \tag{3}$$

where k is the Boltzmann constant and q is the charge of an electron. Eq. (3) is valid only when $V_f > 3kT/q$, and in addition, ideal diode behaviour was not exhibited until approximately $V_f > 0.4$ V for each diode, at each temperature, where at lower applied forward bias, parallel resistances, or shunt resistance, was present. This shunt resistance may have been caused by defects [4], which can be in the form of diffusion paths along dislocations in the semiconductor [24], or leakage around the edge of the diode walls [25]. As a result, a linear least squares fit was applied to the region $0.5 \leq V_f \leq 0.8$. The saturation current was found to decrease as a function of temperature, from 7.97 pA, 8.05 pA, 8.03 pA, and 7.93 pA (each ± 0.04 pA) at 100 °C, to 10.11 aA ± 0.04 aA, 94.12 aA ± 100.32 aA, 10.12 aA ± 0.06 aA, and 11.80 aA ± 6.96 aA at −20 °C, for D1, D2, D3, and D4 respectively. Fig. 7 presents the ideality factor as a function of temperature.

Across the temperature range 100 °C to 20 °C, the ideality factor was ≈ 2 for each diode. This suggested that recombination within the depletion region was the dominant limiting factor for current between 100 °C and 20 °C [24]. Below 20 °C, the ideality factor of two diodes (D1 and D2) were calculated to be slightly > 2, which exceeds the expected value from the Sah–Noyce–Shockley model [26]. The values > 2 in the present case are not thought to be significant but rather a consequence of noise affecting the current measurements at low temperatures and biases. The calculated ideality factors indicated that recombination current defined the forward current, and such a small temperature dependence excluded tunnelling from significant contribution to the forward current [18].

The measured leakage current, I_r, as a function of applied reverse bias for D1 is shown in Fig. 8. The leakage current for each pixel decreased as a function of decreasing temperature. At the maximum

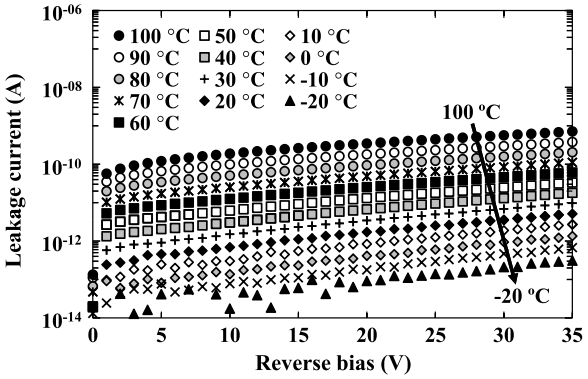

Fig. 8. Leakage current as a function of applied reverse bias in the temperature range 100 °C to −20 °C for D1. Comparable results were obtained for D2, D3, and D4.

applied reverse bias (35 V), the leakage current was measured to be 712.00 pA ± 2.54 pA, 596.19 pA ± 2.19 pA, 591.87 pA ± 2.18 pA, and 671.61 pA ± 2.41 pA at 100 °C; and 0.31 pA, 0.37 pA, 0.36 pA, and 0.33 pA (each ± 0.40 pA) at −20 °C, for D1, D2, D3, and D4 respectively. Fig. 9 presents the leakage current density at an applied reverse bias of 30 V (= 100 kV/cm) as a function of temperature for D1, with comparable results obtained for D2, D3, and D4. The leakage current density, J_R, increased exponentially with increasing temperature (−20 °C to 100 °C). The leakage current densities of each pixel at room temperature were smaller than recently characterised circular $Al_{0.2}Ga_{0.8}As$ (200 μm diameter, 3 μm i layer) devices, where leakage current densities of 40.0 nA cm^{-2} ± 1.4 nA cm^{-2} have been reported at an electric field strength of 100 kV/cm [4]. At the same field strength (equivalent to an applied reverse bias of 30 V for the present devices), and at room temperature, the presently reported $Al_{0.2}Ga_{0.8}As$ 2 × 2 array had a mean pixel leakage current density of 9.0 nA cm^{-2} ± 1.0 nA cm^{-2}. The best leakage current density reported for AlGaAs X-ray photodiodes at room temperature and at an average internal electric field of 100 kV/cm is 2.2 nA cm^{-2} [5], for comparison the leakage current density for high quality 4H-SiC Schottky devices can be ≈ 1 pA cm^{-2} [27].

Leakage current stability with time was measured for each diode as a function of temperature in order to identify the maximum temperature suitable for the X-ray photon counting measurements discussed in Section 3.3. Each pixel was reverse biased at 30 V and its leakage current was measured every 30 s for 1020 s. The applied reverse bias was then reduced to 0 V for a 1 min resting period, and the process repeated 5 times; the results for D1 can be seen in Fig. 10. The devices were

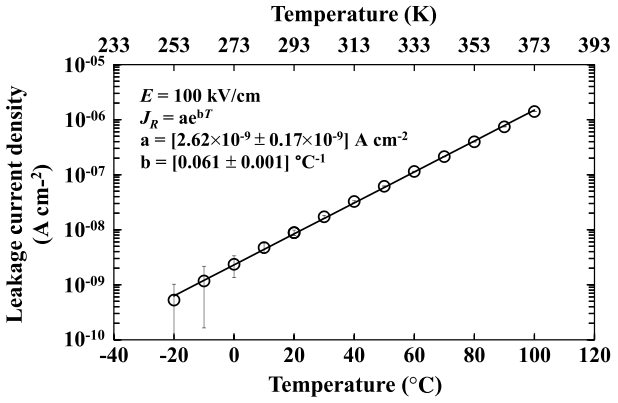

Fig. 9. Measured leakage current density, J_R, at a 100 kV/cm average internal electric field, E, as a function of temperature for D1. A linear least squared fit has been applied, with the line of best fit plotted of the form $J_R = aT + c$, where a has the units of A cm^{-2}, and b units °C^{-1}.

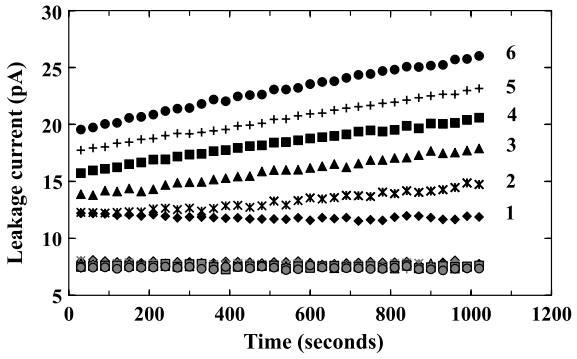

Fig. 10. Leakage current as a function of time for D1 at an applied reverse bias of 30 V and a temperature of 30 °C (grey shapes) and 40 °C (black shapes). Comparable results were obtained for D2, D3, and D4. The measurements made at 40 °C are numbered in accordance with each repetition of the measurement.

found to be stable at temperatures ≤ 30 °C, but at hotter temperatures, the devices became increasingly unstable with repeated applied reverse bias measurements, as shown in Fig. 10.

3.3. Photon counting X-ray spectroscopy

^{55}Fe X-ray spectra were obtained using the X-ray spectrometer S1 (employing detector D1), S2 (employing detector D2), S3 (employing detector D3), and S4 (employing detector D4), to characterise the X-ray detection performance as a function of temperature for the $Al_{0.2}Ga_{0.8}As$ 2 × 2 array. Each diode was connected, in turn, to the same custom-made low-noise charge-sensitive preamplifier of feedback resistorless design similar to Ref. [28]. The preamplifier used a Vishay 2N4416A Si JFET as the input transistor. In each case, the preamplifier was connected to an Ortec 571A shaping amplifier and an Ortec 927 ASPEC multi-channel analyser (MCA). An ^{55}Fe radioisotope X-ray source (≈176 MBq) emitting characteristic Mn Kα (5.9 keV) and Mn Kβ (6.49 keV) X-rays was placed 5 mm above the $Al_{0.2}Ga_{0.8}As$ array. S1, S2, S3, and S4 were installed inside a TAS Micro MT climatic cabinet throughout the measurements for temperature control and characterised in turn. A thermocouple was placed close to the spectrometer to monitor and ensure temperature equilibrium between the climatic cabinet and the spectrometer. The climatic cabinet was continually purged with dry N_2 (<5% relative humidity) in order to reduce any humidity related effects.

The temperature was initially set to 30 °C. It was then decreased to a minimum temperature of −20 °C, in steps of 10 °C. The spectrometer was allowed to stabilise for 30 min upon reaching each desired temperature in order to ensure thermal equilibrium. A maximum temperature of 30 °C was set due to the diodes' leakage current instability at higher temperatures (see Fig. 10). Spectra were accumulated with S1, S2, S3, and S4 at each temperature, and at each shaping time, τ, (0.5 μs, 1 μs, 2 μs, 3 μs, 6 μs, and 10 μs), with each detector reverse biased (V_{AR}) at 0 V, 10 V, 20 V, and 30 V. The live time limit for each spectrum was 200 s. Gaussian fitting was applied to the detected photopeak from the ^{55}Fe radioisotope X-ray source (Mn Kα = 5.9 keV; Mn Kβ = 6.49 keV), taking into account the relative emission ratio [29] and the relative efficiency of the detector at these energies. The spectra were energy calibrated using the positions of the so called zero energy noise peak and the fitted Mn Kα (5.9 keV) peak, with the assumption of a linear variation of detected and output charge with energy. The impact ionisation coefficients of $Al_{0.2}Ga_{0.8}$ as a function of average internal electric field were calculated and indicated that the diodes were operating within the non-avalanche regime [30]. The FWHM at 5.9 keV was measured for all obtained spectra and the associated uncertainty of the fitting calculated; Fig. 11 presents obtained spectra at the maximum (30 °C) and minimum (−20 °C) investigated temperatures for the X-ray spectrometer, S1, at the maximum investigated applied reverse bias (30 V) of the detector, D1.

The low energy tailing seen in Fig. 11 was attributed to partial charge collection of charge created in the non-active layers of the detector [31]. The amount of low energy tailing can be quantified by the valley-to-peak (V/P) ratio, which was calculated for each X-ray spectrometer across the investigated temperature range (30 °C to −20 °C), using the ratio between the number of counts at 3.5 keV and 5.9 keV. The V/P ratio was found to improve (i.e. decrease) as a function of applied reverse bias of the detector for each spectrometer investigated. For the spectrometer S1 (detector D1), at the maximum temperature investigated (30 °C), the V/P ratio was calculated to be 0.15 ± 0.02 with no reverse bias (0 V) applied to the detector, and 0.05 ± 0.01 with 30 V applied reverse bias, at a shaping time of 2 μs. Comparable results were obtained for the spectrometers S2, S3, and S4. The V/P ratio reported here, was better than that previously reported for AlGaAs devices (0.08 at room temperature [2,4]), but not as good when compared to recently reported GaAs 10 μm i layer devices (0.03 at −20 °C [18]). The V/P ratio for each detector bias did not change as a function of temperature within the measured uncertainty, this was likely due to the small temperature range investigated (30 °C to −20 °C).

Fig. 12 presents the measured FWHM at 5.9 keV as a function of shaping time for each spectrometer at 20 °C. The measured energy resolution (FWHM at 5.9 keV) was better than previously reported $Al_{0.2}Ga_{0.8}As$ X-ray photodiodes at room temperature. The best previously reported energy resolution for non-avalanche $Al_{0.2}Ga_{0.8}As$ X-ray detectors (200 μm diameter; 3 μm i layer) was 1.06 keV FWHM at 5.9 keV at room temperature at an average internal electric field strength of 33 kV/cm [4]. The devices reported in Ref. [4] were circular single pixel mesa photodiodes. Using the presently reported devices, a FWHM at 5.9 keV = 0.86 keV ± 0.06 keV was measured under the same conditions with the best performing spectrometer, S2. Additionally, an improved energy resolution (FWHM at 5.9 keV) was measured across the entire temperature range. The best energy resolution (FWHM at 5.9 keV) achieved in Ref. [4] at 0 °C was 0.86 keV and the best at −20 °C was 0.83 keV, at an average electric field strength of 100 kV/cm. Under the same conditions, the best energy resolution measured with the present detectors was 0.72 keV ± 0.06 keV (0.74 keV, 0.73 keV, and 0.77 keV for S1, S3, and S4 respectively, each ± 0.06 keV) at 0 °C and 0.72 keV ± 0.06 keV (0.75 keV, 0.74 keV, and 0.76 keV for S1, S3, and S4 respectively, each ± 0.06 keV) at −20 °C, for the best performing spectrometer reported here, S2. As the epitaxial wafer material of the $Al_{0.2}Ga_{0.8}As$ array used in the present work was the same as that used for the single pixels in Ref. [4], the improved energy resolution now reported is thus attributable to subtle improvements in device fabrication and processing techniques, and in the front-end of the preamplifier. Fig. 13 presents the measured FWHM at 5.9 keV at the optimum shaping time as a function of temperature for the spectrometer, S1, with the photodiode,

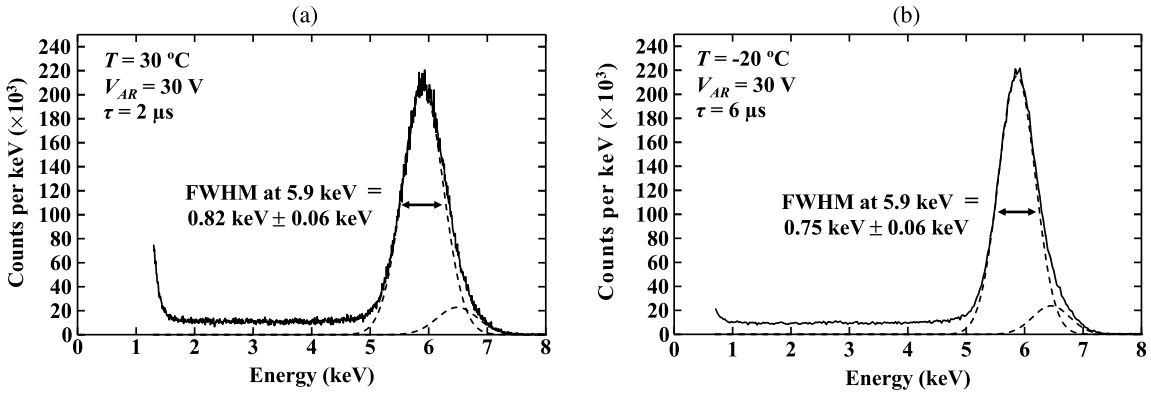

Fig. 11. ^{55}Fe X-ray spectra accumulated with the $Al_{0.2}Ga_{0.8}As$ p^+–i–n^+ mesa photodiode, D1, based X-ray spectrometer, S1, at (a) 30 °C (30 V applied reverse bias and 2 µs shaping time) and (b) −20 °C (30 V applied reverse bias and 6 µs shaping time). The fitted Mn Kα (5.9 keV) and Mn Kβ (6.49 keV) peaks have been plotted (dashed lines). The accumulated spectra have been normalised into counts per 1 keV in order to account for the differing channel widths.

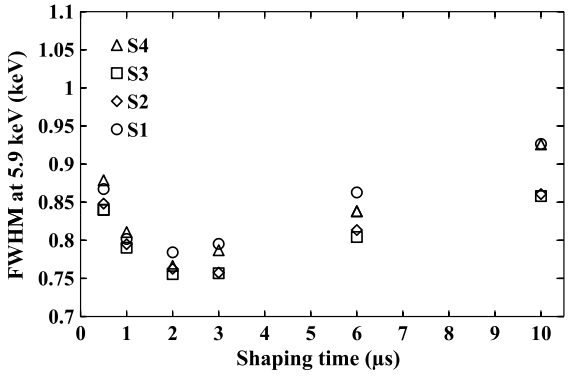

Fig. 12. Measured FWHM at 5.9 keV as a function of shaping time for the $Al_{0.2}Ga_{0.8}As$ based spectrometers S1 (circles), S2 (diamonds), S3 (squares), and S4 (triangles), at room temperature (20 °C) at an applied reverse bias of 30 V.

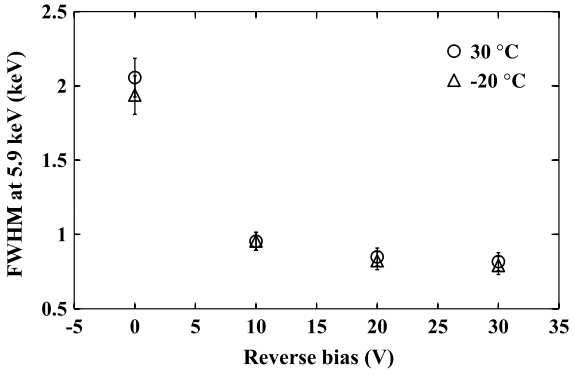

Fig. 14. Measured FWHM at 5.9 keV for S1 as a function of applied reverse bias for the detector, D1, at 30 °C (circles) and −20 °C (triangles) at a shaping time of 2 µs. Comparable results were obtained for S2, S3, and S4.

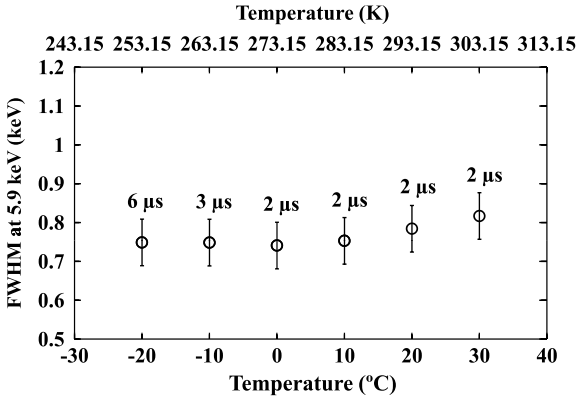

Fig. 13. Measured FWHM at 5.9 keV as a function of temperature for the spectrometer S1. ^{55}Fe X-ray spectra were accumulated with the detector D1 at an applied reverse bias of 30 V, with the optimal shaping time at each temperature plotted.

D1, operated at a reverse bias of 30 V (100 kV/cm) at the best shaping time investigated. The energy resolutions (FWHM at 5.9 keV) achieved at a fixed shaping time of 2 µs across the reverse bias range investigated are presented in Fig. 14 at both 30 °C and −20 °C. The figures show that the change in temperature had little effect on the energy resolution achievable with the spectrometer. Comparable results obtained for the spectrometers S2, S3, and S4.

3.4. Noise analysis

The energy resolution of a non-avalanche semiconductor detector coupled to a charge sensitive preamplifier is influenced by three sources of noise [32]: the Fano noise, which accounts for the stochastic processes in the creation of charge carriers upon absorption of an X-ray [33], the electronic noise, which arises from the detector and preamplifier electronics [34], and any incomplete charge collection noise (including charge trapping) [35]. The fundamental Fano-limited energy resolution (FWHM) at 5.9 keV was calculated to be 132 eV for $Al_{0.2}Ga_{0.8}As$ at room temperature, assuming a Fano factor of 0.12 and an electron–hole pair creation energy of 4.43 eV [4]. Since the measured energy resolution of the spectrometer was greater than the calculated fundamental Fano-limited energy resolution, there were clearly significant noise contributions beyond the statistical generation of charge carries termed the Fano noise.

In a photon counting photodiode X-ray spectrometer, the electronic noise, due to the preamplifier and the detector itself, consists of parallel white noise, series white noise (including the induced gate drain current noise), $1/f$ series noise, and dielectric noise [2]. The leakage current of the detector and the input Junction Field-Effect Transistor (JFET) of the preamplifier give rise to the parallel white noise [18]. The capacitances at the input of the spectrometer, including the detector and the input JFET [18], give rise to the series white noise. Lossy dielectrics in proximity to the input of the spectrometer give rise to the dielectric noise.

Parallel white noise is proportional to the shaping time, τ. Series white noise is inversely proportional to τ. $1/f$ series noise, dielectric

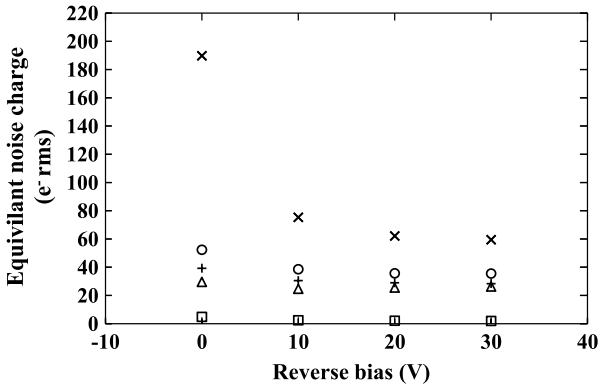

Fig. 15. Equivalent remaining noise contributions of the $Al_{0.2}Ga_{0.8}As$ detector spectrometer, S1, as a function of applied reverse bias of the detector, D1, at the optimum shaping time (2 μs), and at 20 °C. Quadratic sum of the unknown dielectric noise (e.g. stray dielectrics) and any incomplete charge collection noise (crosses); series white noise (circles); known dielectric noise (plus signs); parallel white noise (triangles); $1/f$ series noise (squares). Comparable results were obtained for S2, S3, and S4.

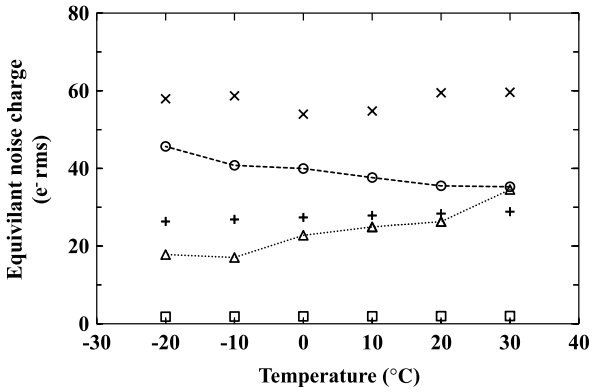

Fig. 16. Calculated remaining noise contributions of the $Al_{0.2}Ga_{0.8}As$ based spectrometer S1 at an applied reverse bias of 30 V and at a shaping time of 2 μs, as a function of temperature: quadratic sum of the unknown dielectric noise and incomplete charge collection noise (crosses); series white noise (circles); known dielectric noise (plus signs); parallel white noise (triangles); $1/f$ series noise (squares). Comparable results were obtained for S2, S3, and S4. The dashed lines are guides for the eyes only.

noise, Fano noise, are τ invariant. Incomplete charge collection noise is also τ invariant, except in extreme cases. The noise contributions can be calculated by applying a multidimensional least squares estimation method to the FWHM at 5.9 keV measured as a function of shaping time [36]. The different noise contributions of each spectrometer (S1, S2, S3, and S4) were investigated as a function of reverse bias applied to the detector and as a function of temperature, in the temperature range 30 °C to −20 °C. Fig. 15 presents the noise contributions as a function of detector applied reverse bias, at 20 °C, and at the optimum shaping time, for the $Al_{0.2}Ga_{0.8}As$ based spectrometer S1 (employing detector D1). It is useful to consider the dielectric noise in two parts: known origin dielectric noise (e.g. contributions arising from the detector and JFET themselves) and unknown origin dielectric noise (e.g. arising from the dielectrics of stray capacitances in proximity to the preamplifier input). The combined contribution of the unknown origin dielectric noise and incomplete charge collection noise at 5.9 keV was calculated by subtracting in quadrature the calculated Fano noise at 5.9 keV, $1/f$ noise, and known dielectric noise from the total shaping time invariant noise contribution.

The quadratic sum of the unknown (e.g. stray) dielectric noise and incomplete charge collection noise decreased as a function of increased applied reverse bias of the detector, from 190 e^- rms ENC at 5.9 keV at 0 V, to 60 e^- rms ENC at 5.9 keV at 30 V. This decrease in noise contribution as a function of increased applied reverse bias, assuming the noise from unknown lossy dielectrics was independent of reverse bias [37], was attributed to the reduction in charge trapping noise (the prime constituent of incomplete charge collection noise broadening the energy resolution). The change in the detector's known dielectric noise as a consequence of the changing detector capacitance was taken into account in calculating the known dielectric noise contributions, and was thus also taken into account in the calculation of the unknown (e.g. stray) dielectric noise.

A quantitative estimate of the reduction of charge trapping noise as a function of increased applied bias was made by subtracting, in quadrature, the unknown dielectric noise and incomplete charge collection noise at an applied reverse bias of 30 V, from the unknown dielectric noise and incomplete charge collection noise at no applied reverse bias (0 V). The incomplete charge collection noise was reduced by 180 e^- rms ENC at 5.9 keV when the detector, D1, was operated at 30 V in comparison to 0 V reverse bias at 20 °C. The majority of this reduction occurred at low magnitude (<20 V) reverse biases; increasing the reverse bias from 20 V to 30 V reduced the incomplete charge collection noise by only 18 e^- rms ENC at 5.9 keV at 20 °C. As an applied reverse bias > 30 V was not investigated, a definite value for the incomplete charge collection noise at 30 V cannot be established. However, the rapid decrease in incomplete charge collection noise which occurred as the applied reverse bias was increased in magnitude towards 30 V, suggests that any incomplete charge collection noise at 30 V was small compared with the total dielectric noise in this condition. The calculated equivalent noise contributions present in S1 as a function of temperature, at an applied reverse bias of 30 V, and at a shaping time of 2 μs, are presented in Fig. 16. The quadratic sum of the unknown dielectric noise and incomplete charge collection noise was the largest noise contribution across all temperatures investigated, and remained approximately constant with temperature (60 e^- rms ENC at 5.9 keV and 58 e^- rms ENC at 5.9 keV, at 30 °C and −20 °C respectively, with the detector reverse biased at 30 V in each case). The parallel white noise decreased with decreasing temperature (from 35 e^- rms ENC at 5.9 keV at 30 °C, to 18 e^- rms at 5.9 keV at −20 °C, with the detector reverse biased at 30 V in each case), resulting from the decreased JFET and detector leakage current with decreasing temperature (see Fig. 8). The series white noise contribution increased with decreasing temperature (35 e^- rms ENC at 5.9 keV to 46 e^- rms ENC at 5.9 keV at 30 °C and −20 °C respectively, with the detector reverse biased at 30 V in each case); this could not be explained solely by the detector's depletion capacitance, which remained approximately constant within the temperature range (100 °C to −20 °C). However, the series white noise not only depends on the total capacitance, but also the capacitive matching between the input JFET and the input load [38]. Therefore, the decreased series white noise with increased temperature may be attributed to a better capacitive match between the input JFET and the input load at higher temperatures.

4. Discussion

The ternary compound semiconductor $Al_xGa_{1-x}As$ has been investigated as a potential material for X-ray detection since 1995 [1]. The relatively wide bandgap of $Al_xGa_{1-x}As$ (e.g. 1.67 eV for $x = 0.2$) [7], in addition to the relatively large X-ray linear attenuation coefficient of $Al_xGa_{1-x}As$ (e.g. 787.8 cm^{-1} for $Al_{0.2}Ga_{0.8}As$ cf. 346.4 cm^{-1} for Si, at 5.9 keV) makes $Al_xGa_{1-x}As$ a promising candidate for X-ray spectroscopy in high temperature and intense radiation environments. Potential space missions which would benefit from a high temperature and/or radiation hard X-ray spectrometer include missions to study the Jovian [13,14] or Saturnian [15] aurorae, the surface of Mercury [39], and the X-ray emissions from Jupiter's Galilean moons [16]. However,

at present, Si is still the most commonly used detector material for X-ray spectroscopy in planetary science and astronomy. For example, the Mercury imaging X-ray spectrometer (MIXS) on the BepiColombo Mercury Planetary Orbiter (MPO) still uses Si as the detecting material [40]. This results in MPO requiring a complex design to protect its instruments from radiation damage and high temperatures; for example, in the case of MIXS, temperatures of −40 °C or below are required for the detector [40] and the spacecraft is expected to experience temperatures up to 350 °C during its mission.

Even when employing shielding and cooling, Si X-ray detectors can still degrade. For example, given the expected radiation intensity during 1 year of BepiColombo's operational lifetime, the MIXS energy resolution is expected to degrade from 100 eV FWHM at 1 keV, to almost 200 eV FWHM at 1 keV [39]. Such degradation in performance puts significant limits on future space mission objectives and mission lifetimes. In some cases, radiation shielding is possible to protect electronics, but detectors must necessarily be exposed to the radiation that they are required to measure, and besides this, greater radiation shielding would increase the mass of future spacecraft and consequently, increase the cost. It is therefore essential that potentially radiation hard materials such as $Al_xGa_{1-x}As$ are investigated and developed. Furthermore, instrumentation made from radiation hard materials could allow X-ray spectrometers to survive for longer periods than conventional instrumentation in intense radiation environments (e.g. missions to study the Jovian radiation environment). As such, the durability of radiation hard X-ray spectrometer improves humanity's ability to investigate such environments thoroughly. In addition, the reduced or eliminated cooling requirements of wide bandgap semiconductor detectors, bring reductions in the mass, volume, and power consumption of spacecraft, enabling more instruments (or cheaper missions) to be flown.

Aside from the promising high temperature and intense radiation tolerance of $Al_xGa_{1-x}As$ in comparison to Si [10–12], the greater X-ray linear attenuation coefficients of $Al_xGa_{1-x}As$ (e.g. 787.8 cm^{-1} for $Al_{0.2}Ga_{0.8}As$ cf. 346.4 cm^{-1} for Si, at 5.9 keV) [9] results in a greater detection efficiency, given the same detector structure. One benefit of this is that given the same detector structure, an increased detection efficiency would allow for shorter X-ray spectra accumulation times, given the same X-ray photon flux, and would consequently increase the number of possible X-ray spectra accumulations within a given mission's lifetime. However, at the moment, Si detectors can be much thicker (e.g. 500 μm [41]) than AlGaAs detectors.

Until now, despite continued efforts, only single pixel $Al_xGa_{1-x}As$ X-ray spectrometers have been reported, with progress hampered by poor quality material and low device yields. However, for the first time, it has been demonstrated here that yields are now sufficient such that small (2 × 2) mesa pixel arrays can be produced, with good enough quality that they are suitable for photon counting X-ray spectroscopy. Uniformity in electrical characteristics and measured energy resolution across each pixel has been demonstrated, in addition to the best measured energy resolution so far reported for AlGaAs X-ray photodiodes at 20 °C (0.86 keV FWHM at 5.9 keV cf. 1.06 keV FWHM at 5.9 keV for Ref. [4] at 20 °C). As the epitaxial wafer material of the $Al_{0.2}Ga_{0.8}As$ single pixels in Ref. [4] was the same as that used in the present work, the improved energy resolution now reported was attributable in part to subtle improvements in device fabrication and processing techniques. These may have aided in the reduction of leakage current density (9.0 nA cm^{-2} ± 1.0 nA cm^{-2} cf. 40.0 nA cm^{-2} ± 1.4 nA cm^{-2} for Ref. [4] at 100 kV/cm and 20 °C). Improvements to the front-end of the preamplifier also contributed to the improved energy resolution, through reductions in the dielectric noise contribution. Since the stray dielectric noise of the X-ray spectrometers reported here still accounts for 60 e^- rms ENC at 5.9 keV at 20 °C; implementing further ways to improve the front end electronics, such as directly wirebonding the photodiodes to the input JFETs, could further improve the energy resolution [36]. As such, the improvement in energy resolution reported here should be seen as an incremental step towards further improving the energy resolution obtained with $Al_xGa_{1-x}As$ X-ray spectrometers.

It should be noted that the energy resolution presently reported is still modest when compared with those measured using GaAs detectors and state-of-the-art Si detectors. For instance, a 5 × 5 GaAs diode array (200 μm diameter, 40 μm i layer) has been previously investigated for X-ray detection: when coupled to ultra-low-noise front end electronics, an energy resolution (FWHM at 5.9 keV) of 266 eV was reported at room temperature [42]. An hexagonal Silicon Drift Detector (SDD) with an energy resolution (FWHM at 5.9 keV) of 141 eV at room temperature when coupled to ultra-low-noise CMOS readout electronics has also been reported [43], and a Si Depleted P-channel Field Effect Transistor (DEPFET) detector, has a reported energy resolution (FWHM at 5.9 keV) of 134 eV [44].

Although the energy resolutions achieved with AlGaAs are not yet as good as with some other more developed materials, it is important to note that useful scientific contributions can still be made by X-ray spectrometers with modest energy resolution. The D-CIXS (Demonstration of a Compact Imaging X-ray Spectrometer) on SMART-1, which measured Ti Kα (4.51 keV) X-ray fluorescence of material on the lunar surface from orbit for the first time in 2005 (reported in 2009 [45]), had an energy resolution of 420 eV FWHM [45]. As such, a photon counting X-ray spectrometer with similar or better energy resolution, that is also tolerant of temperature and radiation hard would likely find much use in future missions to harsh environments.

5. Conclusions and further work

A 2 × 2 square pixel $Al_{0.2}Ga_{0.8}As$ p^+–i–n^+ mesa X-ray photodiode array (each photodiode area 200 μm by 200 μm, 3 μm i layer) has been electrically characterised across the temperature range 100 °C to −20 °C. In addition, each pixel has been characterised as a detector for photon counting X-ray spectroscopy across the temperature range 30 °C to −20 °C.

The depletion layer width, when each pixel was fully depleted (≥26 V applied reverse bias), was found to be independent of temperature within the investigated range (100 °C to −20 °C). At the maximum temperature studied (100 °C), the leakage current remained <1 nA for each pixel and decreased as a function of decreasing temperature across the temperature range 100 °C to −20 °C. A mean leakage current for the four pixels of 0.34 pA ± 0.4 pA was measured at −20 °C when operated at the maximum applied reverse bias (35 V).

The mean FWHM at 5.9 keV achieved using the devices as the detectors in an X-ray spectrometer was 0.80 keV ± 0.06 keV at 30 °C (shaping time of 2 μs), 0.77 keV ± 0.06 keV at 20 °C (shaping time of 2 μs), and 0.75 keV ± 0.06 keV at −20 °C (shaping time of 6 μs). The measured energy resolution at 20 °C (0.77 keV ± 0.06 keV) is the best so far reported for AlGaAs X-ray photodiodes at that temperature. Previously reported energy resolutions for non-avalanche AlGaAs X-ray detectors range from 1.07 keV FWHM at 5.9 keV [17] to 1.27 keV FWHM at 5.9 keV [2] at room temperature.

In future work, characterisation of thicker $Al_{0.2}Ga_{0.8}As$ devices will be reported, where thicker devices should result in lower measured capacitances, and consequently, reduced series white noise, $1/f$ noise, and dielectric noise. In addition, AlGaAs of various Al fractions will be characterised and reported, and efforts will be made to fabricate arrays with larger numbers of pixels.

Acknowledgements

This work was in part supported by Science and Technology Facilities Council, UK, Grants ST/M004635/1 and ST/P001815/1. M.D.C.W. acknowledges funding received in the form of a Ph.D. scholarship from University of Sussex, UK. A.M.B. acknowledges funding from the Leverhulme Trust, UK, in the form of a 2016 Philip Leverhulme Prize. The authors are grateful to B. Harrison, R. J. Airey, and S. Kumar at the EPSRC National Centre for III–V Technologies for material growth and fabrication.

References

[1] J. Lauter, D. Protić, A. Förster, H. Lüth, Nucl. Instrum. Methods Phys. Res. A 356 (1995) 324.
[2] A.M. Barnett, G. Lioliou, J.S. Ng, Nucl. Instrum. Methods Phys. Res. A 774 (2015) 29.
[3] A. Silenas, J. Pozela, K. Pozela, L. Dapkus, V. Juciene, Nucl. Instrum. Methods Phys. Res. A 563 (2006) 21.
[4] M.D.C. Whitaker, S. Butera, G. Lioliou, A.M. Barnett, J. Appl. Phys. 122 (2017) 034501.
[5] A.M. Barnett, J.E. Lees, D.J. Bassford, J. Instrum. 8 (2013) P10014.
[6] A. Silenas, A. Miller, J. Pozela, K. Pozela, L. Dapkus, V. Juciene, Nucl. Instrum. Methods Phys. Res. A 633 (2011) S62.
[7] L. Berger, Semiconductor Materials, frist ed. CRC Press, Boca Raton, 1996.
[8] G. Bertuccio, R. Casiraghi, IEEE Trans. Nucl. Sci. 50 (2003) 175.
[9] B.L. Henke, E.M. Gullikson, J.C. Davis, At. Data Nucl. Data Tables 54 (1993) 181.
[10] A.W. Walker, S. Heckelmann, T. Tibbits, D. Lackner, A.W. Bett, F. Dimroth, Sol. Energy Mater. Sol. Cells 168 (2017) 234.
[11] S. Yoshida, K. Mitsui, T. Oda, Y. Yukimoto, Japan. J. Appl. Phys. 21 (1982) 27.
[12] M. Yamaguchi, J. Appl. Phys. 78 (1995) 1476.
[13] G.R. Gladstone, J.H. Waite, D. Grodent, W.S. Lewis, F.J. Crary, R.F. Elsner, M.C. Weisskopf, T. Majeed, J.M. Jahn, A. Bhardwaj, J.T. Clarke, D.T. Young, M.K. Dougherty, S.A. Espinosa, T.E. Cravens, Nature 415 (2002) 1000.
[14] W.R. Dunn, G. Branduardi-Raymont, R.F. Elsner, M.F. Vogt, L. Lamy, P.G. Ford, A.J. Coates, G.R. Gladstone, C.M. Jackman, J.D. Nichols, I.J. Rae, A. Varsani, T. Kimura, K.C. Hansen, J.M. Jasinski, J. Geophys. Res. Space Phys. 121 (2016) 2274.
[15] G. Branduardi-Raymont, A. Bhardwaj, R.F. Elsner, P. Rodriguez, Astron. Astrophys. 510 (2010) A73.
[16] R.F. Elsner, B.D. Ramsey, J.H. Waite, P. Rehak, R.E. Johnson, J.F. Cooper, D.A. Swartz, Icarus 178 (2005) 417.
[17] A.M. Barnett, D.J. Bassford, J.E. Lees, J.S. Ng, C.H. Tan, J.P.R. David, Nucl. Instrum. Methods Phys. Res. A 621 (2010) 453.
[18] G. Lioliou, M.D.C. Whitaker, A.M. Barnett, J. Appl. Phys. 122 (2017) 244506.
[19] S.M. Sze, Physics of Semiconductor Devices, third ed. John Wiley & Sons, New Jersey, 2006.
[20] S. Adachi, Properties of aluminium gallium arsenide, in: EMIS Datareviews Series 7 INSPEC, The Institution of Electrical Engineers, London, 1993.
[21] R.A. Stradling, P.C. Klipstein, Growth and Characterisation of Semiconductors, first ed. IOP Publishing Ltd, Bristol, 1991.
[22] A.M. Barnett, J.E. Lees, D.J. Bassford, J.S. Ng, C.H. Tan, R.B. Gomes, Nucl. Instrum. Methods Phys. Res. A 626 (2011) 25.
[23] A. Sellai, Proc. IEEE International Conference on Semiconductor Electronics, Johor, Malaysia, 2008, pp. 267-270.
[24] A. Luque, Handbook of Photovoltaic Science and Engineering, second ed. John Wiley & Sons, Chichester, 2011.
[25] T. Soga, Nanostructured materials for solar energy conversion, first ed. Elsevier, Amsterdam, 2006.
[26] C. Sah, R.N. Noyce, W. Shockley, Proc. IRE 45 (1957) 1228.
[27] G. Bertuccio, S. Caccia, D. Puglisi, D. Macera, Nucl. Instrum. Methods Phys. Res. A 652 (2011) 193.
[28] G. Bertuccio, P. Rehak, D. Xi, Nucl. Instrum. Methods Phys. Res. A 326 (1993) 71.
[29] U. Schötzig, Appl. Radiat. Isot. 53 (2000) 469.
[30] X.G. Zheng, P. Yuan, X. Sun, G.S. Kinsey, A.L. Holmes, B.G. Streetman, J.C. Campbell, IEEE J. Quantum Electron. 36 (2000) 1168.
[31] G. Kalinka, Nucl. Instrum. Methods Phys. Res. Sect. B 88 (1994) 470.
[32] G.W. Fraser, X-Ray Detectors in Astronomy, first ed. Cambridge University Press, New York, 1989.
[33] G. Bertuccio, IEEE Solid State Circuits Mag. 4 (2012) 36.
[34] G. Lioliou, A.M. Barnett, Nucl. Instrum. Methods Phys. Res. A 801 (2015) 63.
[35] A. Owens, A. Peacock, Nucl. Instrum. Methods Phys. Res. A 531 (2004) 18.
[36] G. Bertuccio, A. Pullia, Rev. Sci. Instrum. 64 (1993) 3294.
[37] A.M. Barnett, J.E. Lees, D.J. Bassford, J.S. Ng, Nucl. Instrum. Methods Phys. Res. A 673 (2012) 10.
[38] G. Bertuccio, A. Pullia, G. De Geronimo, Nucl. Instrum. Methods Phys. Res. A 380 (1996) 301.
[39] G.W. Fraser, J.D. Carpenter, D.A. Rothery, J.F. Pearson, A. Martindale, J. Huovelin, J. Treis, M. Anand, M. Anttila, M. Ashcroft, J. Benkoff, P. Bland, A. Bowyer, A. Bradley, J. Bridges, C. Brown, C. Bulloch, E.J. Bunce, U. Christensen, M. Evans, R. Fairbend, M. Feasey, F. Giannini, S. Hermann, M. Hesse, M. Hilchenbach, T. Jorden, K. Joy, M. Kaipiainen, I. Kitchingman, P. Lechner, G. Lutz, A. Malkki, K. Muinonen, J. Näränen, P. Portin, M. Prydderch. J. San Juan, E. Sclater, E. Schyns, T.J. Stevenson, L. Strüder, M. Syrjasuo, D. Talboys, P. Thomas, C. Whitford, S. Whitehead, Planet. Space Sci. 58 (2010) 79.
[40] P. Majewski, L. Andricek, A. Bähr, G.D. Vita, B. Günther, K. Hermenau, M. Hilchenbach, T. Lauf, P. Lechner, G. Lutz, D. Miessner, M. Porro, J. Reiffers, R. Richter, G. Schaller, M. Schnecke, F. Schopper, H. Soltau, A. Stefanescu, R. Strecker, L. Strüder, J. Treis, IEEE Trans. Nucl. Sci. 59 (2012) 2479.
[41] C.E. Schlemm, R.D. Starr, G.C. Ho, K.E. Bechtold, S.A. Hamilton, J.D. Boldt, W.V. Boynton, W. Bradley, M.E. Fraeman, R.E. Gold, J.O. Goldsten, J.R. Hayes, S.E. Jaskulek, E. Rossano, R.A. Rumpf, E.D. Schaefer, K. Strohbehn, R.G. Shelton, R.E. Thompson, J.I. Trombka, B.D. Williams, Space Science Reviews 131 (2007) 393.
[42] A. Owens, M. Bavdaz, A. Peacock, A. Poelaert, H. Andersson, S. Nenonen, H. Sipila, L. Tröger, G. Bertuccio, J. Appl. Phys. 90 (2001) 5376.
[43] G. Bertuccio, M. Ahangarianabhari, C. Graziani, D. Macera, Y. Shi, A. Rachevski, I. Rashevskaya, A. Vacchi, G. Zampa, N. Zampa, P. Bellutti, G. Giacomini, A. Picciotto, C. Piemonte, J. Instrum. 10 (2015) P01002.
[44] J. Müller-Seidlitz, R. Andritschke, A. Bähr, N. Meidinger, S. Ott, R.H. Richter, W. Treberspurg, J. Treis, (2016) SPIE Conference on Astronomical Telescopes and Instrumentation.
[45] B.M. Swinyard, K.H. Joy, B.J. Kellett, I.A. Crrawford, M. Grande, C.J. Howe, V.A. Fernandes, O. Gasnault, D.J. Lawrence, S.S. Russell, M.A. Wieczorek, B.H. Foing, Planet. Space Sci. 57 (2009) 744.